Nanoscale

PAPER

View Article Online
View Journal | View Issue

Cite this: *Nanoscale*, 2024, **16**, 9911

A high density nanopore 3-triangulene kagome lattice†

Pedro Elias Priori Spalenza, [a] Fábio Arthur Leão de Souza, [b] Rodrigo G. Amorim, [c] Ralph H. Scheicher *[d] and Wanderlã Luis Scopel [a]

Nanopore-containing two-dimensional materials have been explored for a wide range of applications including filtration, sensing, catalysis, energy storage and conversion. Triangulenes have recently been experimentally synthesized in a variety of sizes. In this regard, using these systems as building blocks, we theoretically examined 3-triangulene kagome crystals with inherent holes of ~12 Å diameter and a greater density array of nanopores ($\geq 10^{13}$ cm^{-2}) compared to conventional 2D systems. The energetic, electronic, and transport properties of pristine and B/N-doped 3-triangulene kagome crystals were evaluated through a combination of density functional theory and non-equilibrium Green's function method. The simulated scanning tunneling microscopy images clearly capture electronic perturbation around the doped sites, which can be used to distinguish the pristine system from the doped systems. The viability of precisely controlling the band structure and transport properties by changing the type and concentration of doping atoms is demonstrated. The findings presented herein can potentially widen the applicability of these systems that combine unique electronic properties and intrinsically high-density pores, which can pave the way for the next generation of nanopore-based devices.

Received 2nd March 2024,
Accepted 4th April 2024

DOI: 10.1039/d4nr00910j

rsc.li/nanoscale

1. Introduction

Since the isolation of graphene,[1] two-dimensional (2D) systems have paved the way for designing and fabricating novel materials. Recently, the production of nanoflakes[2] based on aromatic rings has received great attention due to the possibility of fabricating tailored materials for applications of 2D nanodevices. In this sense, graphene nanoflakes with a triangular shape, called *n*-triangulene[3–6] (*n* being the number of benzoic rings on a side), have been used as a building block for creating more complex structures.[7–9]

The synthesis of unsubstituted triangulenes is a difficult task due to the presence of unpaired electrons and due to their highly reactive edges. However, Allinson[10] and Taylor[11] overcame these issues with the addition of substituents, which permitted their stabilization and synthesis. Recently, experimental breakthroughs have opened routes to the on-surface synthesis (such as on Cu(111), NaCl(100), Xe(111), and Au (111)) of unsubstituted triangulenes utilizing different precursors and techniques, allowing the synthesis of molecules,[3] dimers,[7] chains[8] and nanostars.[9]

A promising way to tune the electronic and magnetic properties of triangulenes is through doping and edge passivation.[12,13] Kan *et al.*[14] have studied isolated 3-triangulene and demonstrated that it is possible to manipulate the occupation of π orbitals by replacing the central carbon atom with nitrogen or boron. They have also explored triangulene crystals and showed through the use of density functional theory (DFT) calculations that N-doping tunes the magnetic order from antiferromagnetic to ferromagnetic. In addition, Chen *et al.* have reported a facile synthesis of replacing the carbon edges of 4-triangulene with three oxygen–boron–oxygen (OBO) units, and the results suggest that these kinds of molecules hold promising potential for optical applications and can be a route to creating OBO-doped 2D materials.[15]

2D crystals derived from substituted[12,16–20] and non-substituted[21,22] triangulenes have also been explored. Steiner *et al.*[18] successfully fabricated a 2D covalent kagome network architecture based on carbonyl-functionalized pores on the Au (111) surface. The system was characterized through a combination of scanning tunneling microscopy (STM) and DFT calculations, which showed that it is weakly bound to the sub-

[a]*Departamento de Física, Universidade Federal do Espírito Santo – UFES, Vitória, ES, Brazil. E-mail: pedro.spalenza@edu.ufes.br*
[b]*Instituto Federal de Educação, Ciência e Tecnologia do Espírito Santo – IFES, Ibatiba, ES, Brazil. E-mail: fabio.souza@ifes.edu.br*
[c]*Departamento de Física, ICEx, Universidade Federal Fluminense – UFF, Volta Redonda, RJ, Brazil. E-mail: rgamorim@id.uff.br*
[d]*Division of Materials Theory, Department of Physics and Astronomy, Uppsala University, Box 516, SE-751 20 Uppsala, Sweden. E-mail: ralph.scheicher@physics.uu.se*

† Electronic supplementary information (ESI) available. See DOI: https://doi.org/10.1039/d4nr00910j

strate and its electronic structure is kept unperturbed. Interestingly, a periodic membrane with intrinsic holes can be produced using triangulenes as building blocks. In particular, nanopores in 2D materials have potential applications in DNA, protein and biomolecule sensing,[23–25] desalination,[26–28] the petrochemical industry[29,30] and others.[20,31,32]

In this work, through DFT combined with non-equilibrium Green's function (NEGF), we explored the structural, electronic, and electronic transport properties of pristine and B/N-doped 3-triangulene kagome lattices. A systematic investigation of the central carbon atom of triangulenes substituted with B or N was performed *via* calculation of the formation energy, which is governed by an exothermic process. STM images were obtained and the results show the difference between the doped and pristine systems. The results also show that band dispersion around the Fermi level can be precisely controlled by varying the type of dopant and its concentration. Finally, the zero-bias transmission of the B/N-doped systems shows an increase in the number of transmission channels at the Fermi level compared to the pristine system. Thus, our findings suggest these systems as highly promising potential candidates for nanopore-based devices.

2. Methodology

Atomic structure optimization, energetic stability, and electronic property calculations were performed using DFT.[33,34] The exchange–correlation energy was described within the generalized gradient approximation (GGA) proposed by Perdew, Burke, and Ernzerhof (PBE),[35] as implemented in Quantum ESPRESSO.[36,37] The interaction between ions and valence electrons was described by projector augmented wave pseudopotentials (PAW),[38,39] and the energy cutoff was set to 650 eV. All structures were relaxed until Hellmann–Feynman forces acting on each atomic component were smaller than 0.05 eV Å^{-1}. An orthorhombic unit cell of 29.83 Å × 17.22 Å × 15.00 Å dimensions was used with a sufficiently large vacuum gap in the *z*-direction in order to avoid interactions between periodic images. The Brillouin zone integration was performed using the Monkhorst–Pack scheme[40] with 5 × 5 × 1 grids.

We also carried out DFT calculations as implemented in the SIESTA[41,42] package. The core electrons were described by norm-conserving Troullier–Martins pseudopotentials,[43] and a double-zeta polarized (DZP) basis set[44] was considered. A real-space mesh cutoff (300 Ry) and 2 × 2 × 1 *k*-point grids were used. The Tersoff–Hamann STM[45] model was used, where the tip is assumed to be of s-orbital type, and the tunneling current is proportional to the local density of states (LDOS). In this approach, the sum is over all Kohn–Sham states in the energy windows (E_F, E_F − V) and (E_F, E_F + V) for occupied and unoccupied states, respectively, in which the isosurfaces of the LDOS can be correlated with them at a constant height. V is the applied bias and E_F is the Fermi energy.

Transport calculations were carried out with the TranSIESTA code,[46,47] which combines DFT and NEGF, and the schematic model used is shown in Fig. 1(b). For solving the electronic transport problem, Green's function was used and is defined as below:

$$\mathcal{G}(E) = [E \times S_S - H_S - \Sigma_L(E) - \Sigma_R(E)]^{-1} \quad (1)$$

where the terms S_S and H_S are the overlap and Hamiltonian matrices of the scattering region, respectively. The left (right) self-energy ($\Sigma_{L(R)}$) gives the electrode contribution inside the scattering region. Thus, the energy-resolved electronic transmission, $T(E)$, which represents the probability of an electron coming in from the left electrode to reach the right electrode, and passing through the scattering region, can be written as follows:

$$T(E) = \mathrm{Tr}\left[\Gamma_L(E)G(E)\Gamma_R(E)\mathcal{G}^{\dagger}(E)\right] \quad (2)$$

where the coupling matrices are defined as $\Gamma_\alpha = i[\Sigma_\alpha - \Sigma_\alpha^{\dagger}]$, and $\alpha \equiv \{L, R\}$. $\mathcal{G}\left(\mathcal{G}^{\dagger}\right)$ is the retarded (advanced) Green's function.

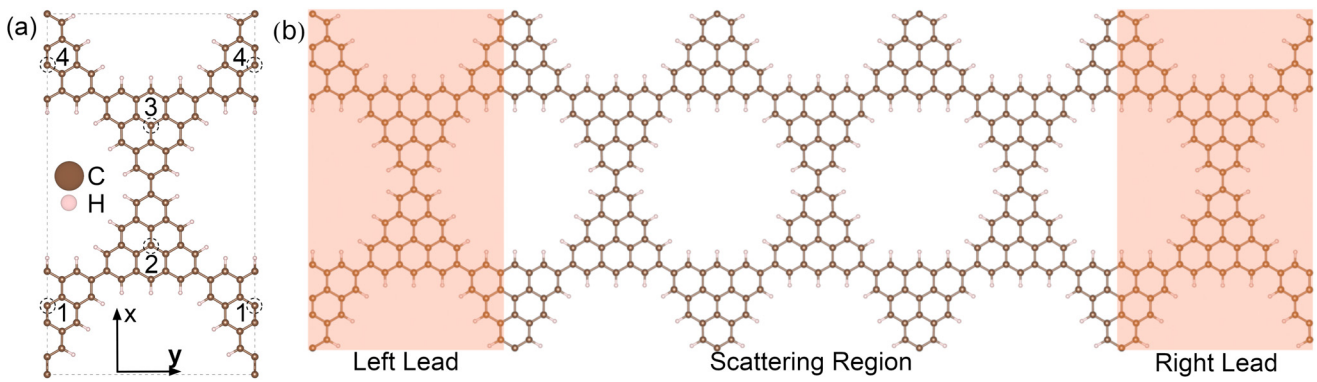

Fig. 1 (a) Fully relaxed geometry of the rectangular unit cell of the 3-triangulene kagome, where doping sites are indicated by numbers 1–4. Brown and light pink color spheres represent the C and H atoms, respectively. (b) Schematic setup of electronic transport along the *y*-direction. The dimensions of the scattering region (electrodes) are 29.83 Å (29.83 Å) wide and 51.66 Å (17.22 Å) long. The scattering regions for each of the studied structures are depicted in Fig. S2 and S3 in the ESI.†

We have carried out zero-bias calculations, which lead to zero electrical currents. Further details can be found elsewhere.[46,47]

3. Results

The schematic crystalline structure of the 3-triangulene kagome is shown in Fig. 1(a), and the atomic sites that will be doped with either boron or nitrogen are highlighted by dashed circles and labeled with the numbers 1–4, where dashed grey lines show the unit cell. Interestingly, regarding the graphene domain, sites 1 and 3 (2 and 4) belong to sublattice A (B). These doping sites were motivated by success in multiple experiments in similar systems.[16–19,48] From the 3-triangulene relaxed atomic structure, we found that the C–C bond lengths vary from 1.40 Å to 1.43 Å, and C–H bond length was found to be 1.09 Å. The nanopore density was determined by calculating the number of pores per unit area. The density of 3.89×10^{13} cm^{-2} for the 3-triangulene kagome represents a notably high value for pore density.[49]

Fig. 2 shows the electronic band structure of the 3-triangulene kagome (black solid lines), where one notes flat bands appearing roughly at ±0.2 eV, which are ascribed to carbon p_z orbitals (as can be seen in Fig. S1 of the ESI†). Additionally, a Dirac cone around the Fermi level along the Y → Γ direction (corresponding to the zigzag direction of the crystals) is also observed. These features are typical signatures of the kagome lattice, as previously reported.[22]

Wang *et al.* have experimentally demonstrated that the substitution of the central carbon atom of 3-triangulene on a metal surface (Ag and Au) can substantially modify the electronic and magnetic properties of the system.[48] In addition, Anindya *et al.* found[21] that B/N doping on the triangulene kagome lattice permitted control of the electronic/magnetic properties of 3-triangulene crystals. In this context, the energetic stability of substitutional defects in the 3-triangulene kagome was explored and their formation energy per atom (E_{form}) was calculated using the equation:

$$E_{form} = \left(E_X - E_{prist} + n(\mu_C - \mu_X)\right)1/n_a \quad (3)$$

where E_X (E_{prist}) stands for the total energy of the X (X = B or N atoms)-doped (pristine) system, n is the number of doped atoms, n_a is the number of atoms in the unit cell and μ_X (μ_C) represents the chemical potential of the doped (carbon) atoms. Carbon's chemical potential was determined using the CH_4 molecule, while those of boron and nitrogen were derived from the B bulk and N_2 molecule, respectively.

Table 1 shows that for all studied concentrations and for both dopants (B and N), the system formation is governed by an exothermic process. A linear increment of the formation energy with the number of doping atoms for both dopant species is observed (as presented in Fig. S4 of the ESI†), following the same tendency of previous reports.[50,51] For the B-doped system, the formation energy varies from −5.4 meV per atom up to −22.0 meV per atom, while N doping varies from −41.9 meV per atom to −169.0 meV per atom. This verifies that doping induces a small structural disorder of the C–C (<0.04 Å) and C–H distances far from the doped sites compared to pristine ones, where the internuclear separations of the B-doped (N-doped) systems C–B (C–N) are 1.47 (1.39) Å, which agree very well with B- and N-doped graphene.[52]

Fig. 2(a)–(d) show the band structures of the 3-triangulene kagome doped with boron atoms at atomic sites 1–4, as labeled in Fig. 1. B-doping induces a systematic shift of bands toward higher energies in comparison with the pristine one

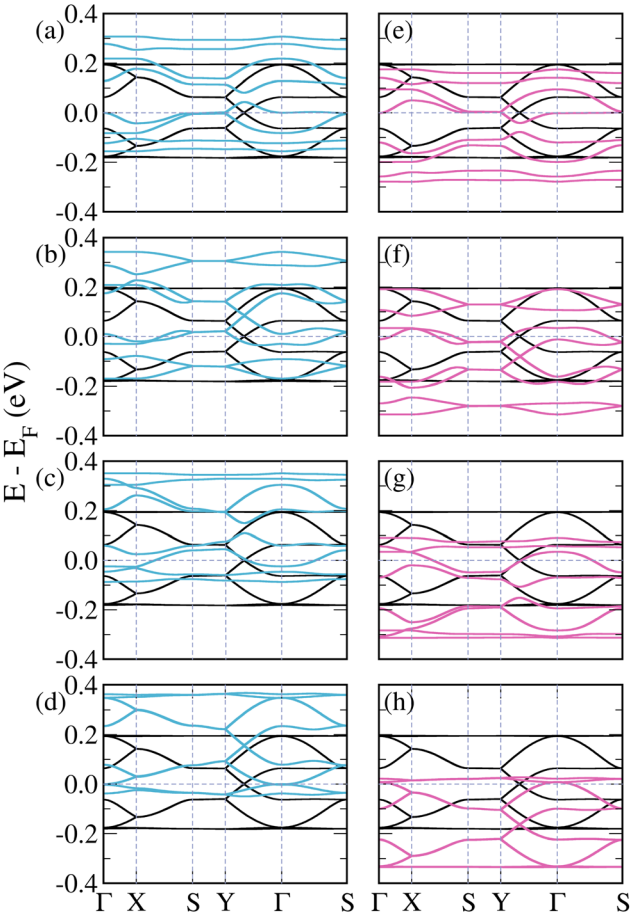

Fig. 2 Band structures of pristine (black lines) and doped 3-triangulene kagome lattices: (a)–(d) doping atomic sites 1–4 with boron (light blue lines) and (e)–(h) doping sites 1–4 with nitrogen (pink lines); as labeled in Fig. 1.

Table 1 Formation energy per atom for the doped systems, where negative values of energy indicate an exothermic process

	E_{form} (meV per atom)	
Number of dopants	B-doping	N-doping
1	−5.4	−41.9
2	−11.0	−84.3
3	−16.7	−126.8
4	−22.0	−169.0

(black curves) with increasing doping concentration (from Fig. 2(a)–(d)), resulting in a p-doping-like effect. In all cases, the number of bands crossing the Fermi level increases. Interestingly, the Dirac cone (Y to Γ) is preserved, as observed in Fig. 2(b) and (d), whereas in Fig. 2(a) and (c) it is opened. In the case of N-doping, one observes a systematic shift of the bands to lower energy compared to the pure ones, which characterizes the n-doping effect. For the Y–Γ path, one notes in Fig. 2(f) and (h) that the Dirac cone is preserved, while in Fig. 2(e) and (g) the Dirac cone opens. As a result, for both B- and N-doping, an opening of the Dirac cone is observed when the number of doped sites in sublattices A and B are different. On the other hand, when the numbers of doped sites in sublattices A and B are equal, the Dirac cone is preserved, with only a shift toward higher (lower) energies in the B-doped (N-doped) case. These results suggest that by varying the kind and concentration of doping, band dispersion around the Fermi level can be precisely controlled. It is important to highlight that for the case where the unit cell is doped twice, there are two possible configurations (as shown in the ESI, Fig. S5†). Fig. 2(b) and (f) only show the case where sites 1 (sublattice A) and 2 (sublattice B) are doped; the other case (when sites 1 (sublattice A) and 3 (sublattice A) are doped) is shown in the ESI, Fig. S6†. A similar trend of opening and closure of the Dirac cone was observed for pristine graphene.[53]

To better understand the effect of B/N doping on the surface at the atomic scale, Fig. 3 shows simulated STM images for the 3-triangulene kagome and its doped counterparts, the most energetically favorable ones (4B-doped and 4N-doped). We simulated the filled (empty) states by integrating charge density from the Fermi level to −1.0 (+1.0) eV, and the images were obtained considering the constant-height mode. The aforementioned energy ranges are where dopant energy levels appear (as shown in Fig. S7†). Fig. 3(a) and (b) show the pristine 3-triangulene kagome and 4B-doped systems for occupied states, while Fig. 3(c) and (d) present the pristine and 4N-doped systems for an unoccupied state, respectively. The STM images for occupied and unoccupied states differ in the linkage between the two neighboring triangles. For the undoped ones, we note two well-defined charge lobules for occupied state 3 (a), and in the case of unoccupied state 3 (c), there are four lobules linking the triangles. Fig. 3(b) shows a B-doped system, where the three brightest spots in the center of the triangles appear as a continuum triangular shape, once a boron atom, by Bader's analysis,[54,55] donates one electron to each of its first neighbors, as expected due to carbon possessing higher electronegativity. On the other hand, for the N-doped system, the effect is different once the N atom is the acceptor and C is the donator, as shown in Fig. 3(d). The results clearly show that doped systems can be distinguished from pristine ones in both situations, as the bright patterns in the vicinity of doped sites change significantly in shape. Our results of the simulated STM image for the freestanding 3-triangulene kagome are locally comparable with triangulene dimers on Au (111) surface.[7]

The focus will now be on the 3-triangulene kagome lattice's electronic transport properties and how 4B- and 4N-doping affects them. Fig. 4(b) presents the zero bias transmission curves for pristine (black curve), 4N-doped (pink curve), and 4B-doped lattices (light blue). For the pristine case, we observe two quite symmetrical peaks around the Fermi level. As expected from the band structure analysis, N-doping (B-doping) induces a shift of the two corresponding peaks toward lower (higher) energies. As a result, an increase in the number of transmission channels at the Fermi level is observed for both doped cases. Additionally, we observed the emergence of two new peaks in the transmission spectra of the 4B-doped system at −0.045 eV and 0.334 eV, and one new peak at 0.035 eV for the 4N-doped case. To understand the origin of

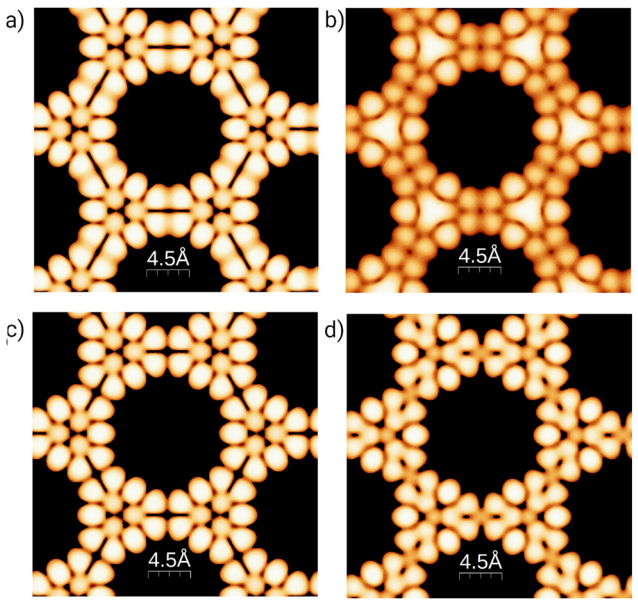

Fig. 3 Simulated STM images of occupied states (−1.0 eV up to E_F): (a) pristine and (b) B-doped 3-triangulene kagome lattices. Unoccupied state (E_F up to +1.0 eV) STM images are shown for the pristine 3-triangulene kagome (c) and N-doped (d) one.

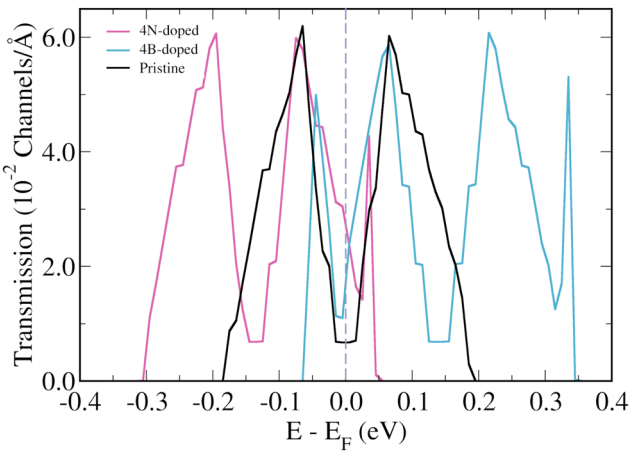

Fig. 4 Energy resolved zero bias transmission for the pristine (black lines), B-doped (light blue lines), and N-doped lattices (pink lines) of 3-triangulene kagome.

these new peaks in the transmission of doped systems, one needs to keep in mind that in the band structure of the pristine system, there are two degenerated flat bands at −0.18 eV and another two at +0.19 eV, and that these flat bands do not contribute to transport initially. However, in the 4B-doped band structure (Fig. 2(d)), one can verify that the bands, which correspond to the flat bands of the pristine system, become less energetically localized and their degeneracy is lifted around the Gamma point. For the 4N-doped case, the same effect described above for the 4B-doped is observed for the band at 0.035 eV. Such circumstances are responsible for the two (one) extra peaks in the 4B-doped (4N-doped) transmission when compared to the pristine one.

Finally, spin-polarized calculations were also performed and used to estimate the Néel Temperature with the mean-field approximation given by eqn (4):[56,57]

$$T_N^{MF} = \left(-\frac{2}{3\kappa_B}\Delta E\right) 1/n_C \quad (4)$$

where ΔE is the difference in energy between the anti-ferromagnetic ground state and the non-polarized system and n_C is the number of C atoms in the unit cell. From eqn (4), we calculated a Néel temperature (T_N) of 47.71 K for the 3-triangulene crystals. Therefore, this result indicates that this system will be non-magnetic at room temperature. Hence, in this work, we focused only on exploring the electronic and transport properties controlled through B/N-doping and refrained from studying the magnetic properties of 3-triangulene, which can be addressed in future studies.

4. Conclusions

Energetic, electronic and transport properties of pristine, boron-, and nitrogen-doped 3-triangulene crystals were assessed by a combination of DFT and NEGF methods. Different concentrations of dopants were considered and our results reveal that the formation energies of all doped systems are governed by an exothermic process and scale linearly in energy with the doping concentration. From the structural characterization of the systems, simulated STM images clearly show that doped systems can be distinguished from the pristine one. From an electronic point of view, the band dispersion around the Fermi level can be controlled by the doping and concentration type. For the highest concentration, transmission curves shift toward higher (lower) energies for B (N) doping, and the number of transmission channels at the Fermi level increases with respect to the pristine system. Triangulene kagome lattices' unique electronic properties and the feasibility of manipulating them through doping make this system a promising candidate for use in next-generation nano-sized bio sensors.

Conflicts of interest

There are no conflicts to declare.

Acknowledgements

The authors acknowledge the financial support from the Brazilian agencies CAPES, CNPq, and FAPES (TO – 1043/2022) and the computational resources of CENAPAD-SP. WLS and RGA thank CNPq for the financial support (301648/2017-4 and 421227/2018-4; and (2535/2017-1, 437182/2018-5 and 313076/2020-0, respectively). RGA also acknowledges the financial support from FAPERJ, grant numbers E-26/010.101126/2018, E-26/210.077/2022 and E-26/202.699/2019. This study was financed in part by the Coordenação de Aperfeiçoamento de Pessoal de Nível Superior – Brasil (CAPES) – Finance Code 001.

References

1 K. S. Novoselov, A. K. Geim, S. V. Morozov, D.-e. Jiang, Y. Zhang, S. V. Dubonos, I. V. Grigorieva and A. A. Firsov, *Science*, 2004, **306**, 666–669.
2 A. Casanova, R. Rincón, J. Muñoz, C. Ania and M. Calzada, *Fuel Process. Technol.*, 2021, **212**, 106630.
3 N. Pavliček, A. Mistry, Z. Majzik, N. Moll, G. Meyer, D. J. Fox and L. Gross, *Nat. Nanotechnol.*, 2017, **12**, 308–311.
4 S. Mishra, K. Xu, K. Eimre, H. Komber, J. Ma, C. A. Pignedoli, R. Fasel, X. Feng and P. Ruffieux, *Nanoscale*, 2021, **13**, 1624–1628.
5 J. Su, M. Telychko, P. Hu, G. Macam, P. Mutombo, H. Zhang, Y. Bao, F. Cheng, Z.-Q. Huang, Z. Qiu, *et al.*, *Sci. Adv.*, 2019, **5**, eaav7717.
6 S. Mishra, D. Beyer, K. Eimre, J. Liu, R. Berger, O. Groning, C. A. Pignedoli, K. Mullen, R. Fasel, X. Feng, *et al.*, *J. Am. Chem. Soc.*, 2019, **141**, 10621–10625.
7 S. Mishra, D. Beyer, K. Eimre, R. Ortiz, J. Fernández-Rossier, R. Berger, O. Gröning, C. A. Pignedoli, R. Fasel, X. Feng, *et al.*, *Angew. Chem.*, 2020, **132**, 12139–12145.
8 S. Mishra, G. Catarina, F. Wu, R. Ortiz, D. Jacob, K. Eimre, J. Ma, C. A. Pignedoli, X. Feng, P. Ruffieux, *et al.*, *Nature*, 2021, **598**, 287–292.
9 J. Hieulle, S. Castro, N. Friedrich, A. Vegliante, F. R. Lara, S. Sanz, D. Rey, M. Corso, T. Frederiksen, J. I. Pascual, *et al.*, *Angew. Chem., Int. Ed.*, 2021, **60**, 25224–25229.
10 G. Allinson, R. J. Bushby, J. L. Paillaud, D. Oduwole and K. Sales, *J. Am. Chem. Soc.*, 1993, **115**, 2062–2064.
11 G. Allison, R. J. Bushby, M. V. Jesudason, J. L. Paillaud and N. Taylor, *J. Chem. Soc., Perkin Trans. 2*, 1997, 147–156.
12 Y. Jing and T. Heine, *J. Am. Chem. Soc.*, 2018, **141**, 743–747.
13 T. Li and Y. Jing, *J. Phys. Chem. C*, 2022, **126**, 17836–17843.
14 E. Kan, W. Hu, C. Xiao, R. Lu, K. Deng, J. Yang and H. Su, *J. Am. Chem. Soc.*, 2012, **134**, 5718–5721.
15 X. Chen, D. Tan, J. Dong, T. Ma, Y. Duan and D.-T. Yang, *J. Phys. Chem. Lett.*, 2022, **13**, 10085–10091.

16 M. Bieri, S. Blankenburg, M. Kivala, C. A. Pignedoli, P. Ruffieux, K. Müllen and R. Fasel, *Chem. Commun.*, 2011, **47**, 10239–10241.
17 F. Schlutter, F. Rossel, M. Kivala, V. Enkelmann, J.-P. Gisselbrecht, P. Ruffieux, R. Fasel and K. Mullen, *J. Am. Chem. Soc.*, 2013, **135**, 4550–4557.
18 C. Steiner, J. Gebhardt, M. Ammon, Z. Yang, A. Heidenreich, N. Hammer, A. Görling, M. Kivala and S. Maier, *Nat. Commun.*, 2017, **8**, 14765.
19 G. Galeotti, F. De Marchi, E. Hamzehpoor, O. MacLean, M. Rajeswara Rao, Y. Chen, L. Besteiro, D. Dettmann, L. Ferrari, F. Frezza, *et al.*, *Nat. Mater.*, 2020, **19**, 874–880.
20 Y. Jing, Z. Zhou, W. Geng, X. Zhu and T. Heine, *Adv. Mater.*, 2021, **33**, 2008645.
21 K. N. Anindya and A. Rochefort, *Carbon Trends*, 2022, **7**, 100170.
22 R. Ortiz, G. Catarina and J. Fernández-Rossier, *2D Mater.*, 2022, **10**, 015015.
23 L. Xue, H. Yamazaki, R. Ren, M. Wanunu, A. P. Ivanov and J. B. Edel, *Nat. Rev. Mater.*, 2020, **5**, 931–951.
24 J. Prasongkit, E. de Freitas Martins, F. A. De Souza, W. L. Scopel, R. G. Amorim, V. Amornkitbamrung, A. R. Rocha and R. H. Scheicher, *J. Phys. Chem. C*, 2018, **122**, 7094–7099.
25 F. A. de Souza, R. G. Amorim, W. L. Scopel and R. H. Scheicher, *Phys. Chem. Chem. Phys.*, 2019, **21**, 24884–24890.
26 A. Raza, J. Z. Hassan, A. Mahmood, W. Nabgan and M. Ikram, *Desalination*, 2022, **531**, 115684.
27 Z. Cao, V. Liu and A. B. Farimani, *Nano Lett.*, 2019, **19**, 8638–8643.
28 G.-R. Xu, J.-M. Xu, H.-C. Su, X.-Y. Liu, H.-L. Zhao, H.-J. Feng, R. Das, *et al.*, *Desalination*, 2019, **451**, 18–34.
29 K. Su, W. Wang, S. Du, C. Ji and D. Yuan, *Nat. Commun.*, 2021, **12**, 3703.
30 Y. Yang, L. Li, R.-B. Lin, Y. Ye, Z. Yao, L. Yang, F. Xiang, S. Chen, Z. Zhang, S. Xiang, *et al.*, *Nat. Chem.*, 2021, **13**, 933–939.
31 S. Rashidi, J. A. Esfahani and A. Rashidi, *Renewable Sustainable Energy Rev.*, 2017, **73**, 1198–1210.
32 S. Zhang, P. Zhang, A. Xie, S. Li, F. Huang and Y. Shen, *Electrochim. Acta*, 2016, **212**, 912–920.
33 P. Hohenberg and W. Kohn, *Phys. Rev.*, 1964, **136**, B864.
34 W. Kohn and L. J. Sham, *Phys. Rev.*, 1965, **140**, A1133.
35 J. P. Perdew, K. Burke and M. Ernzerhof, *Phys. Rev. Lett.*, 1996, **77**, 3865.
36 P. Giannozzi, S. Baroni, N. Bonini, M. Calandra, R. Car, C. Cavazzoni, D. Ceresoli, G. L. Chiarotti, M. Cococcioni, I. Dabo, *et al.*, *J. Phys.: Condens. Matter*, 2009, **21**, 395502.
37 P. Giannozzi, O. Andreussi, T. Brumme, O. Bunau, M. B. Nardelli, M. Calandra, R. Car, C. Cavazzoni, D. Ceresoli, M. Cococcioni, *et al.*, *J. Phys.: Condens.Matter*, 2017, **29**, 465901.
38 P. E. Blöchl, *Phys. Rev. B: Condens. Matter Mater. Phys.*, 1994, **50**, 17953.
39 J. J. Mortensen, L. B. Hansen and K. W. Jacobsen, *Phys. Rev. B: Condens. Matter Mater. Phys.*, 2005, **71**, 035109.
40 H. J. Monkhorst and J. D. Pack, *Phys. Rev. B: Solid State*, 1976, **13**, 5188.
41 J. M. Soler, E. Artacho, J. D. Gale, A. García, J. Junquera, P. Ordejón and D. Sánchez-Portal, *J. Phys.: Condens. Matter*, 2002, **14**, 2745.
42 A. García, N. Papior, A. Akhtar, E. Artacho, V. Blum, E. Bosoni, P. Brandimarte, M. Brandbyge, J. I. Cerdá, F. Corsetti, *et al.*, *J. Chem. Phys.*, 2020, **152**, 204108.
43 D. Hamann, M. Schlüter and C. Chiang, *Phys. Rev. Lett.*, 1979, **43**, 1494.
44 J. Junquera, Ó. Paz, D. Sánchez-Portal and E. Artacho, *Phys. Rev. B: Condens. Matter Mater. Phys.*, 2001, **64**, 235111.
45 J. Tersoff and D. R. Hamann, *Phys. Rev. B: Condens. Matter Mater. Phys.*, 1985, **31**, 805.
46 M. Brandbyge, J.-L. Mozos, P. Ordejón, J. Taylor and K. Stokbro, *Phys. Rev. B: Condens. Matter Mater. Phys.*, 2002, **65**, 165401.
47 N. Papior, N. Lorente, T. Frederiksen, A. García and M. Brandbyge, *Comput. Phys. Commun.*, 2017, **212**, 8–24.
48 T. Wang, A. Berdonces-Layunta, N. Friedrich, M. Vilas-Varela, J. P. Calupitan, J. I. Pascual, D. Pena, D. Casanova, M. Corso and D. G. de Oteyza, *J. Am. Chem. Soc.*, 2022, **144**, 4522–4529.
49 S. Su, X. Wang and J. Xue, *Mater. Horiz.*, 2021, **8**, 1390–1408.
50 T. M. Dieb, Z. Hou and K. Tsuda, *J. Chem. Phys.*, 2018, **148**, 241716.
51 M. Yang, L. Wang, M. Li, T. Hou and Y. Li, *AIP Adv.*, 2015, **5**, 067136.
52 P. Rani and V. Jindal, *RSC Adv.*, 2013, **3**, 802–812.
53 H. I. Sirikumara, E. Putz, M. Al-Abboodi and T. Jayasekera, *Sci. Rep.*, 2016, **6**, 19115.
54 G. Henkelman, A. Arnaldsson and H. Jónsson, *Comput. Mater. Sci.*, 2006, **36**, 354–360.
55 W. Tang, E. Sanville and G. Henkelman, *J. Phys.: Condens. Matter*, 2009, **21**, 084204.
56 H. Shi, H. Pan, Y.-W. Zhang and B. I. Yakobson, *Phys. Rev. B: Condens. Matter Mater. Phys.*, 2013, **88**, 205305.
57 P. D. Reyntjens, S. Tiwari, M. L. Van de Put, B. Soree and W. G. Vandenberghe, *2D Mater.*, 2020, **8**, 025009.